Atmospheric Research 218 (2019) 372–384

Contents lists available at ScienceDirect

Atmospheric Research

journal homepage: www.elsevier.com/locate/atmosres

Assessment of extreme precipitation events and their teleconnections to El Niño Southern Oscillation, a case study in the Wei River Basin of China

Rengui Jiang[a,*], Yinping Wang[a], Jiancang Xie[a], Yong Zhao[b,*], Fawen Li[c], Xiaojie Wang[a]

[a] State Key Laboratory of Eco-hydraulics in Northwest Arid Region of China, Xi'an University of Technology, Xi'an 710048, China
[b] State Key Laboratory of Simulation and Regulation of Water Cycle in River Basin, China Institute of Water Resources and Hydropower Research, Beijing 100038, China
[c] State Key Laboratory of Hydraulic Engineering Simulation and Safety, Tianjin University, Tianjin 300072, China

ARTICLE INFO

Keywords:
Extreme precipitation index (EPI)
Spatiotemporal change pattern
El Niño Southern Oscillation
Linear and nonlinear relationships
Wei River Basin (WRB)

ABSTRACT

Extreme precipitation index (EPI) is used to assess the extreme precipitation events, to further monitor and detect climate change impacts. The primary objective of the paper is to assess the extreme precipitation events and their spatiotemporal variability of 14 EPIs, and further investigate the linear and nonlinear relationships between typical EPIs and global climate anomalies El Niño Southern Oscillation (ENSO), using Niño 3.4 and SOI as climate indices, for the period of 1969–2016 in the Wei River Basin (WRB) of China. Observed daily precipitation data from 18 meteorological stations in the WRB were selected to calculate 14 EPIs derived or modified from core indices of the CCI/WCRP Expert Team for Climate Change Detection Monitoring and Indices (ETCCDMI). The trends of EPIs were estimated using Mann-Kendall non-parametric test. The teleconnections of ENSO to EPIs were revealed using principal component analysis (PCA), Pearson's correlation and wavelet analysis. Results indicate that: (1) The change patterns of extreme precipitation events varied for different EPIs and different meteorological stations for the period of 1969–2016 in the WRB. Four EPIs were negative trends dominated, and six EPIs were positive trends dominated, indicating that the extreme precipitation events had mainly increased for the past 48 years. (2) The spatial distributions of seven categories of trends were scattered and irregular for different EPIs and different areas of WRB. However, some of the EPIs had similar spatial distributions of trends. For example, the stations that had increasing trends mainly located at the northern part of WRB, especially in the Jing River Basin (JRB), for six precipitation intensity EPIs except R150, which was stationary trend dominated. (3) The nonlinear teleconnection relationships between typical EPIs and two climate anomalies revealed using wavelet analysis were consistent with linear relationships using correlation analysis. The Niño 3.4 and SOI had similar wavelet coherence but opposite phase difference with PC1 of typical EPIs. The phase differences between Niño 3.4 and PC1 of EPIs were anti-phase dominated, and in-phase dominated between SOI and PC1 of EPIs, indicating that the Niño 3.4 exerted negative climate impacts on the extreme precipitation events in the WRB and vice-versa for SOI. (4) The results should be beneficial to assess the extreme precipitation events, which provide references for the water resources planning and management in the WRB. It is possible to estimate and predict the future extreme precipitation events using climate models and global climate anomalies as potential predictors, which should be further studied in our future work.

1. Introduction

Global and regional weather and climate extremes have severe impacts on human society and environment, which has attached widespread attention for the last few decades, especially for the latter half of the twentieth century (Min et al., 2011). The extreme climate events had increased in both frequency and magnitude (Sun et al., 2016; Utsumi et al., 2011). Climate change and the anthropogenic influences have affected the global climate system and water cycle, with observed global changes in precipitation patterns and intensification of extreme precipitation events such as the torrential rainstorm flood over land areas (Croitoru et al., 2013; Ziegler, 2012). Climate modes indicate that extreme precipitation events will be more frequent (Allan and Soden, 2008). The precipitation extremes have been projected to increase more than the mean precipitation under the future changed climate. However, the mechanism was unclear (Emori, 2005). The Intergovernmental Panel on Climate Change (IPCC) Fifth Assessment Report (AR5) showed that the heavy precipitation events had increased

* Corresponding authors.
E-mail addresses: jrengui@163.com, rgjiang@xaut.edu.cn (R. Jiang), Zhaoyong@iwhr.com (Y. Zhao).

https://doi.org/10.1016/j.atmosres.2018.12.015
Received 11 July 2018; Received in revised form 30 November 2018; Accepted 17 December 2018
Available online 18 December 2018
0169-8095/ © 2018 Elsevier B.V. All rights reserved.

globally, especially in land areas. High confidence showed that mean precipitation in the mid-latitude land areas of the Northern Hemisphere has increased, and the heavy precipitation events have increased in a number of regions, especially after 1951. The extreme precipitation events were projected to increase in the intensity and frequency in many countries and regions around the world using projected simulations of different General Circulation Models (GCMs) and Representative Concentration Pathways (RCPs) (IPCC, 2014). The increasing trends of extreme precipitation events indicate greater risks of flooding, caused severe losses, which has become a universal focus (Jiang et al., 2017a).

Many previous studies have investigated change patterns of extreme precipitation events at different regions, such as, global and regional scales, and in different parts of China (Alexander et al., 2016; Jiang et al., 2017b; Zhang et al., 2001). At global scale, Easterling et al. (2000) reviewed the observed variability and trends in extreme climate events globally including extreme precipitation and temperature events, drought and wet periods, tropical storms and extreme climate indices, which have received widely attention at the latter half of twentieth century. Cavanaugh et al. (2015) studied the probability tail structure to identify the distribution of intense daily precipitation and extremes based on over 22,000 meteorological stations around the world. The results indicated that the probability tail thickness was linked with the precipitation events climatology at different scales. In case of China, Zhai et al. (2005) assessed the trends of seasonal and annual total precipitation and extreme daily precipitation for the period 1951–2000 in China, based on an observed daily precipitation data set of 740 stations. The results showed that the trends of annual total precipitation varied in different regions, mainly significantly decreasing trends in north of China, but significantly increased in western China. However, the precipitation extremes had significantly decreased in some regions such as north China. Zhang et al. (2013) analyzed the spatiotemporal patterns of precipitation extremes using eight precipitation extreme indices for the period of 1960–2005 in China. The results indicate that the northwest of China had a wetting tendency, and several river basins such as Yellow river basin had a drying tendency. The intensification of extreme precipitation events might lead to an increase possibility of precipitation related hazards, such as flood and drought events. At regional scale, Jiang et al. (2017b) investigated the change characteristics of precipitation extremes in Shaanxi province in the northwest of China between two periods of 1954–1983 and 1984–2013 and climate change impacts, using observed daily precipitation data. The results found that the spatial distributions of trends of different precipitation extremes were scattered and unstable. Generally, the precipitation extremes had increasing trends dominated between 1984 and 2013, but not obvious trends between 1954 and 1983, indicating possible climate change impacts on the extreme precipitation events. Wang et al. (2017) examined the spatial and temporal variations of extreme precipitation events and their regional differences during 1961–2014 in the coastal area of China (CAS) using several mathematical and statistical methods. Results indicated that the extreme precipitation events had insignificant tendency, and the abrupt change mainly occurred in the 1970s and 1990s.

To reveal the change mechanism of extreme precipitation events, the paper further investigated the linear and nonlinear teleconnection relationships between extreme precipitation events and global climate anomalies El Niño Southern Oscillation (ENSO), which is one of the coupled atmosphere-ocean phenomenon at nearly 2–7 year scales (Torrence and Webster, 1999). It has been verified that ENSO had great influences on the precipitation patterns mainly in the tropical Pacific, and climate change impacts over the Pacific region and in many areas of the world through global teleconnections (IPCC, 2014). Previous studies have studied the relationships between precipitation extremes and ENSO at different spatial scales, such as different regions of America, (Schubert et al., 2008), (Grimm and Tedeschi, 2009), (Shimizu et al., 2017), Canada (Jiang et al., 2014), China (Li et al., 2011). For example, Grimm and Tedeschi (2009) studied the climate change impacts of ENSO on the frequency of precipitation events using both daily observed precipitation and gridded precipitation data in South America. The results showed that the frequency of precipitation extremes were related to ENSO signals over study area. Specially, significant trends of precipitation extremes were stronger with respect to monthly precipitation trends because ENSO were more sensitive to extremes than mean values of precipitation. Jiang et al. (2014) found that the ENSO had stronger impacts on the Alberta's precipitation mainly in the southern part using aggregate composite analysis. The El Niño and La Niña were mainly correlated to spare and abundant precipitation respectively, especially in southern Alberta. Li et al. (2011) investigated the relationships between ENSO and extreme precipitation events for the period of 1951–2004 in China using observed daily precipitation. The results showed that ENSO exerted influence in extreme precipitation events, which varied for different seasons and regions.

Most previous studies on the long-term climate change mainly focused on trends of mean or total precipitation for the past several decades (Alexander et al., 2016). However, we focused on the extreme precipitation indices (EPIs) based on the observed daily precipitation because the EPIs are more suitable to analyze the change characteristics than mean precipitation. The potential variations of extreme precipitation events are of great importance because they likely exert severe social and economic loss, such as rainstorm and flood events (Schubert et al., 2008). The EPIs have been widely used to reveal the climate effects in previous studies (Jiang et al., 2017b). Especially, joint World Meteorological Organization Commission for Climatology (CCI)/World Climate Research Programme (WCRP) project on Climate Variability and Predictability expect Team on climate change Detection, Monitoring and Indices (ETCCDMI) has proposed a suite of climate extreme indices to monitor climate change impacts. An easy-to-use software package named RClimDex was developed to calculate the EPIs, which is of great convenience for the users.

Few studies delved into the variations and change mechanism of precipitation extremes in Wei River Basin (WRB), the mother river of Shaanxi province and largest branch of the Yellow River in China. The primary objective of this paper is to assess the extreme precipitation events using 14 EPIs as substitutions for the period of 1969–2016 in the WRB, using Mann-Kendall non-parametric method. The linear and nonlinear teleconnection relationships between extreme precipitation events in the WRB and ENSO on a global scale were revealed using principal component analysis (PCA), Pearson's correlation and wavelet analysis. The results should be helpful to reveal the characteristics of extreme precipitation events in the WRB and climate change impacts of ENSO, which provide potential possibility of using global climate anomalies to predict the precipitation extremes in the WRB. Material and methods are described in Section 2, followed by Results in Section 3. Discussion and Conclusions are presented in Section 4 & 5, respectively.

2. Material and methods

2.1. Study area

The WRB locates between 33.68°N-37.39°N latitude and 103.94°W-110.03°W longitude (Fig. 1), situated in the west-central of China. The length of the WRB is 818 km and it covers 135,000 km^2. 44.1% of the WRB area lies in the Gansu province, 6.1% in the Ningxia Hui autonomous region, and the remaining area in the Shaanxi province. The main tributaries of WRB include the Jing River Basin (JRB) and Beiluo River Basin (BRB). The JRB is the largest tributary of WRB, flowing about 455 km generally northwest to the southeast. The BRB is the longest river in Shaanxi province, about 680 km. The main stream of WRB originated from the Gansu province and trends eastward, through Tianshui city in Gansu province, Baoji, Xianyang, Xi'an, Weinan cities in

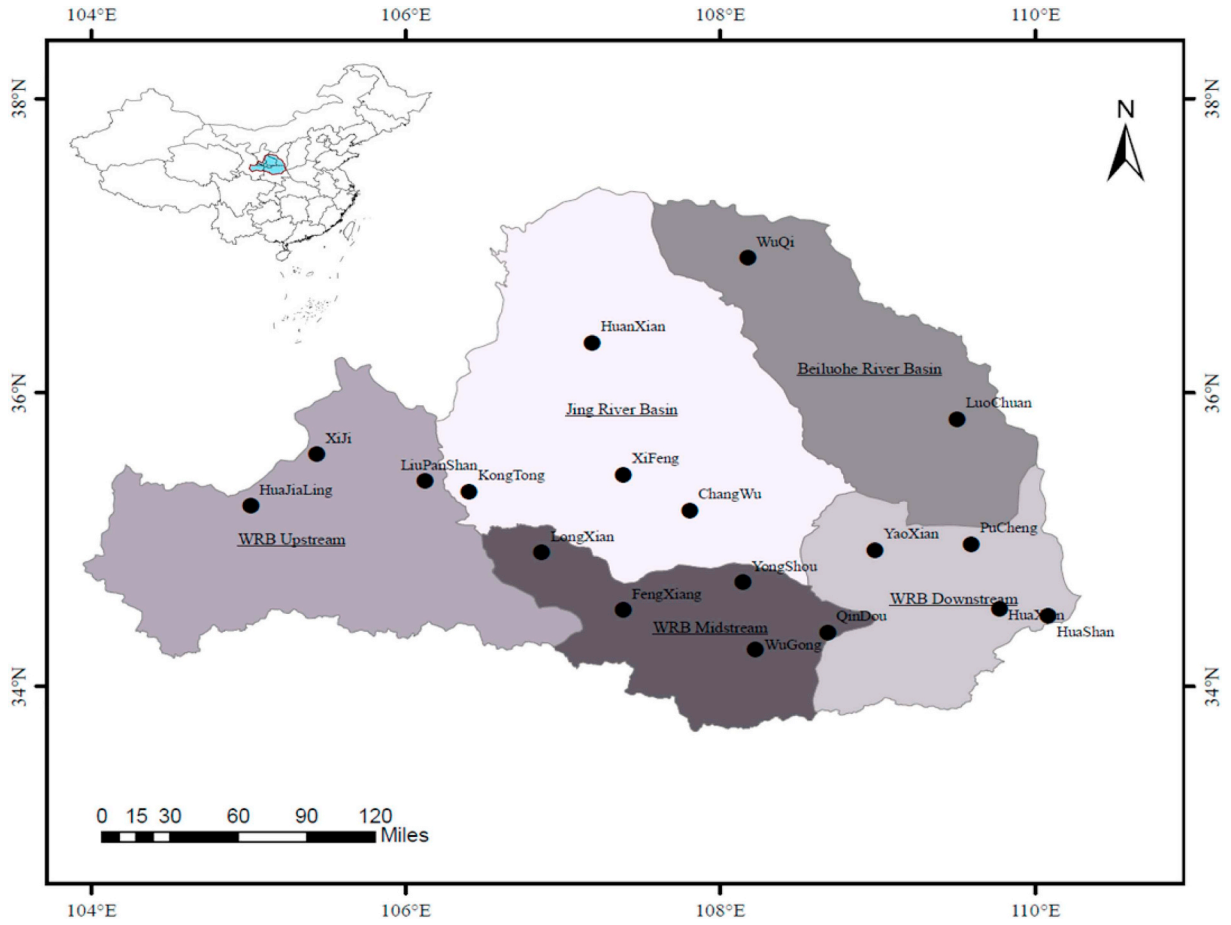

Fig. 1. Locations of study area and 18 meteorological stations.

Shaanxi province. According to the river morphology, the WRB can be divided into five parts (Fig. 1). The upstream of WRB is about 430 km, rising from the Qin Mountains. The midstream of the WRB is located from Baoji gorge to Xianyang, nearly 180 km. The downstream of the WRB is about 208 km, from Xianyang to join the Yellow River.

The meteorological and hydrological features varied for different seasons and regions over the WRB due to the diversity of its multifarious geological, geographic and climate conditions. The annual mean precipitation is about 570 mm for past several decades. > 60% of the annual precipitation centered from July to October. The annual mean natural runoff in the WRB is nearly 10 billion m^3, taking up nearly 17.3% of total natural runoff of Yellow River. However, both precipitation and runoff characteristics varied for different regions, from the upstream to downstream, and from south bank to north bank of WRB, caused severe flood and drought events in the history (Jiang et al., 2013, 2015).

2.2. Climate data

Spatial and temporal variability of the EPIs were analyzed for 18 meteorological stations between 1969 and 2016 in the WRB. The daily precipitation data were downloaded from the China Meteorological Administration (http://data.cma.cn/). Table 1 shows the basic information of 18 stations, which have an irregularly spatial distribution, located at the upstream, midstream, downstream and tributaries of the WRB.

Previous studies showed that the extremes of climate patterns' oscillations such as ENSO had influences on the extreme precipitation events in many regions of the world. ENSO is an irregularly periodic variations in sea surface temperature (SST) and winds over the equatorial Pacific Ocean (IPCC, 2014). The warm and cold phases of ENSO are known as El Niño and La Niña, respectively. Two climate pattern oscillations including Niño 3.4 and SOI were used as substitution of ENSO to reveal the impacts of climate change on the extreme precipitation events in the WRB. The above two indices have been widely used in previous studies, e.g., (Varotsos, 2013; Jiang et al., 2014; Varotsos et al., 2018).

The Niño 3.4 index indicates the regional average equatorial SST over the central tropical Pacific with the regions of 5°S-5°N, 170°W-120°W (Trenberth, 1997). Southern Oscillation is an accompanying atmospheric component of El Niño and La Niña, coupled with the SST between the tropical western and western Pacific Ocean. The SOI index is used to measure the strength of the Southern Oscillation, defined as the normalized monthly Sea Level Pressure (SLP) anomaly between Tahiti (18°S, 150°W) and Darwin (12°S, 131°E) (Ropelewski and Jones, 1987). The Niño 3.4 index was supplied by the National Weather Service Climate Prediction Center (CPC) of National Oceanic and Atmospheric Administration (NOAA). The SOI index was downloaded from Climatic Research Unit (CRU).

2.3. Definition and calculation of EPIs

Fourteen EPIs were defined and used to investigate the extreme precipitation events of WRB in the paper (see Table 2). These EPIs were extracted or modified from the core indices of ETCCDMI. The 14 EPIs were divided into three categories according to the thresholds, including fixed thresholds, stations-related thresholds and non-threshold EPIs. The fixed thresholds EPIs indicate the frequency of the extreme precipitation events, such as, consecutive wet day (CDD), R25mm. The station-related thresholds and non-threshold EPIs represent the

Table 1
Characteristics of the weather stations in Wei River Basin (WRB) used in the study.

No.	WMO code	STNM	Longitude(°E)	Latitude(°N)	Elevation(m)	River basin
1	52,996	HuaJiaLing	105.01	35.23	2450.6	WRB upstream (3 stations)
2	53,903	XiJi	105.43	35.58	1916.5	
3	53,910	LiuPanShan	106.12	35.40	2841.2	
4	57,003	LongXian	106.86	34.91	1018.0	WRB midstream (5 stations)
5	57,049	FengXiang	107.38	34.52	782.6	
6	57,025	YongShou	108.14	34.71	1018.0	
7	57,037	QinDou	108.68	34.37	466.0	
8	57,028	WuGong	108.22	34.25	447.8	
9	57,030	YaoXian	108.98	34.93	710.0	WRB downstream (4 stations)
10	57,034	HuaShan	110.08	34.48	2064.9	
11	57,046	HuaXian	109.77	34.53	335.0	
12	53,948	PuCheng	109.59	34.97	489.0	
13	53,821	HuanXian	107.18	36.34	1255.6	Jing river basin (4 stations)
14	53,915	KongTong	106.40	35.33	1346.6	
15	53,923	XiFeng	107.38	35.44	1421.0	
16	53,929	ChangWu	107.80	35.20	1206.5	
17	53,738	WuQi	108.17	36.92	1331.4	Beiluo river basin (2 stations)
18	53,942	LuoChuan	109.50	35.82	1159.8	

intensity of precipitation, e.g., very wet days (R95p), monthly maximum 1-day precipitation (Rx1day) and simple daily intensity index (SDII).

Eight fixed thresholds EPIs include CDD, consecutive wet day (CWD), and other six indices of precipitation days, i.e., R10mm, R20mm, R25mm, R50mm, R100mm and R150mm. The R10mm and R20mm indicate heavy precipitation and very heavy precipitation, respectively. The R25mm is on behalf of extremely heavy precipitation. The R50mm represents rainstorm. The R100 indicates heavy rainstorm. The last EPI named R150mm is for extreme heavy rainstorm days. The above five fixed thresholds EPIs were transformed to identify and assess the extreme precipitation events. Station-related thresholds EPIs include R95p and R99p, which were defined based on the proportion of annual total runoff when RR > certain proportion. The R95p is 95th proportion, and the R99p is 99th proportion, respectively. Four non-threshold EPIs including Rx1day, monthly maximum consecutive 5-day precipitation (Rx5day), annual total wet-day precipitation (PRCPTOT) and SDII were investigated in the paper. These four EPIs were calculated using the absolute daily precipitation data. More details including the definition and meaning of the EPIs can be found in previous paper (Jiang et al., 2017a, 2017b; Zhang and Yang, 2004).

The EPIs were calculated using the RClimDex software. It can be downloaded from http://etccdi.pacificclimate.org. The RClimDex was developed using R language (Zhang and Yang, 2004). Before using the RClimDex, the observed daily precipitation should go through strict data quality control including determining the unreasonable or missing data, to make the results credible.

2.4. Wavelet coherence and phase difference

Pearson's correlation and wavelet analysis are used to investigate the linear relationships and non-stationary characteristics between EPIs and ENSO. Morlet wavelet was used as the month wavelet because it contained more oscillations. It consists of a plane wave modulated by a Gaussian function (Torrence and Compo, 1998). The Morlet wavelet is defined as $\Psi_0(\eta) = \pi^{-1/4} e^{iw_0\eta} e^{-\eta^2/2}$, where w_0 is the number of oscillations within the wavelet, i and n are the non-dimension time and frequency.

Wavelet coherence $R_n^2(S)$ represent the square of the cross-wavelet spectrum, $W_n^{XY}(s)$, of X and Y, normalized by the smoothed wavelet power, where $\langle\cdot\rangle$ smooth the wavelet spectrum in different time and scale (Torrence and Webster, 1999):

$$R_n^2(s) = \frac{|S\langle s^{-1} W_n^{XY}(s)\rangle|^2}{S\langle s^{-1}|W_n^X(s)|^2\rangle S\langle s^{-1}|W_n^Y(s)|^2\rangle} \quad (1)$$

where $R_n^2(s) \in [0,1]$, and $W_n^{XY}(s) = W_n^X(s) \times W_n^{Y*}(s)$.

n and s indicate the time and scale of wavelet transform, $W_n^X(s)$ and $W_n^Y(s)$ are the wavelet transforms of X and Y. $W_n^{Y*}(s)$ is the complex conjugate of $W_n^Y(s)$ (Torrence and Compo, 1998). The smoothing operator S of $W_n^{XY}(s)$ in numerator and wavelet power spectrum (WPS) in denominator is given as follows (Jevrejeva et al., 2003):

$$S(W) = S_{scale}(S_{time}(W(s,t))) \quad (2)$$

WPS is calculated by the square of wavelet transform absolute value. S_{scale} indicates smoothing along the wavelet scale axis and S_{time} denotes smoothing in time (Torrence and Compo, 1998):

Table 2
Definitions of 14 extreme precipitation indices (EPIs) used in the study.

No.	Acronym	Index name	Definitions	Category	Unit
1	CDD	Consecutive dry days	Maximum number of consecutive days with RR < 1 mm	Fixed thresholds EPIs	Days
2	CWD	Consecutive wet days	Maximum number of consecutive days with RR ≥ 1 mm		days
3	R10mm	Number of heavy precipitation days	Annual count of days when PRCP ≥ 10 mm		Days
4	R20mm	Number of very heavy precipitation days	Annual count of days when PRCP ≥ 20 mm		Days
5	R25mm	Number of extremely heavy precipitation days	Annual count of days when PRCP ≥ 25 mm		Days
6	R50mm	Number of rainstorm days	Annual count of days when PRCP ≥ 50 mm		Days
7	R100mm	Number of heavy rainstorm days	Annual count of days when PRCP ≥ 100 mm		Days
8	R150mm	Number of extreme heavy rainstorm days	Annual count of days when PRCP ≥ 150 mm		Days
9	R95p	Very wet days	Annual total PRCP when RR > 95th percentile	Station-related thresholds EPIs	mm
10	R99p	Extremely wet days	Annual total PRCP when RR > 99th percentile		mm
11	Rx1day	Max 1-day precipitation amount	Monthly maximum 1-day precipitation	Non-threshold EPIs	mm
12	Rx5day	Max 5-day precipitation amount	Monthly maximum consecutive 5-day precipitation		mm
13	PRCPTOT	Annual total wet-day precipitation	Annual total PRCP in wet days (RR ≥ 1 mm)		mm
14	SDII	Simple daily intensity index	Annual total precipitation divided by the number of wet days		mm/day

$$S_{scale}(W)|_s = (W(t,s)c_1 e^{-(t^2/2s^2)})|_s \quad (3)$$

$$S_{time}(W)|_n = (W(t,s)c_2\Pi(0.6s))|_n \quad (4)$$

where C_1, C_2 are the normalized constants, Π is the rectangle function, and 0.6 is the empirically that indicates the scale decorrelation length for the Morlet wavelet. The wavelet phase difference is given as follows:

$$\phi_n(s) = \tan^{-1}(\Im\{\langle s^{-1} W_n^{XY}(s)\rangle\}/\Re\{\langle s^{-1} W_n^{XY}(s)\rangle\}) \quad (5)$$

where $\Im\{\cdot\}$ and $\Re\{\cdot\}$ are the imaginary and real part of wavelet spectra, respectively (Torrence and Webster, 1999).

PCA is a statistical approach which uses an orthogonal transformation to transform a set of observations of possibly related variables to a set of linearly independent variables. It is used in the paper to derive the dominant signals of EPIs from 18 meteorological stations in the WRB. The leading principal components (PCs) that explain majority of signals are selected as substitutions to investigate the relationships between EPIs and ENSO. Details of PCA refer to several previous studies (Jiang et al., 2014; Singh, 2006).

2.5. Mann-Kendall non-parametric test

The Mann-Kendall non-parametric test was used to analyze the trends of the above 14 EPIs, due to its non-parametric characteristic. The Kendall's S of EPIs $X = \{x_1, \ldots, x_i \ldots x_n\}$ is given as follows:

$$S = \sum_{i-1}^{n-1} \sum_{j=i+1}^{n} a_{ij},\ a_{ij} = sign(x_j - s_i) = \begin{cases} 1 & if \quad \Delta x > 0 \\ 0 & if \quad \Delta x = 0 \\ -1 & if \quad \Delta x < 0 \end{cases} \quad (6)$$

where n is the length of X, $\Delta x = x_j - x_i E(S)$ and $Var(S)$ are the mean value and variance of statistic S.

$$E(S) = 0,\ Var(S) = \left[n(n-1)(2n+5) - \sum_{p=1}^{q} t_p(t_p - 1)(2t_p + 5) \right] / 18 \quad (7)$$

S distribution tends to normality if the number of EPIs is bigger than 8 (Yue and Wang, 2002; Hamed, 2009). The standardized Z statistic is defined as follows (Shadmani et al., 2012):

$$Z = \begin{cases} (S-1)/\sqrt{Var(S)} & S > 0 \\ 0 & S = 0 \\ (S+1)/\sqrt{Var(S)} & S < 0 \end{cases} \quad (8)$$

The positive (negative) values of Z indicate increasing (decreasing) trends of EPIs, and $Z = 0$ means stationary. The null-hypothesis at α significance level will be rejected if $|Z| > Z_{1-\alpha/2}$, indicating significant trends in the EPIs. Two α values 5% and 10% are used to detect the significant trends of EPIs in the study. Details of Mann-Kendall non-parametric test method refer to previous study (Jiang et al., 2014; Yue et al., 2002).

3. Results

3.1. General variations of fourteen EPIs

Table 3 and Fig. 2 show the trends of the 14 EPIs of the 18 meteorological stations for the period of 1969–2016 in the WRB using the Mann-Kendall non-parametric test. Table 3 shows the proportions of stations that exhibited different change variation including positive, negative and stationary trends of 14 EPIs. The EPIs were divided into three categories, as introduced in Section 2.3. Fig. 2 is the boxplot of the trends for 14 EPIs based on 18 observed stations' daily precipitation data during 1969–2016 in the WRB. Four red dotted lines in the Fig. 2 indicate that EPIs are statistically significant increase (or decrease) at both 5% and 10% significant levels. The positive values represent increasing trends, and the negative values indicate decreasing trends. The Z statistic value equal to zero indicates that the EPI had stationary trend for the past 1969–2016. The spatial distributions of EPIs trends are presented in Figs. 3–5.

For the past 48 year (1969–2016), more stations were negative trends dominated for four EPIs, i.e., CDD, CWD, R10mm and PRCPTOT, and six EPIs including R25mm, R100mm, R95p, R99p, Rx1day and Rx5day were increasing trends dominated. Coincidentally, stations that had positive trends were equal to those of negative trends for three EPIs, R20mm, R50mm and SDII. R150mm was stationary trends dominated. Only two stations had positive trends, and no stations had negative trend. Other sixteen stations did not have extreme heavy rainstorm days (precipitation ≥ 150 mm) for the period of 1969–2016 in the WRB.

The highest proportion of stations that had positive trends was 61.11% for both R99p and Rx1day, indicating that 11 out of 18 stations had increasing trends, followed by 55.56% for R25mm and R100mm. The CWD and PRCPTOT were negative trends dominated. Only 16.67% (3 out of 18) of stations had positive trends for both EPIs, followed by R10mm (33.33%). The highest proportion of stations that exhibited negative trends was 83.33% for CWD, followed by 77.78% for PRCPTOT and 66.67% for R10mm. In case of R99p, one station had statistically increasing trend at 5% significance level, and four EPIs including R95p, R99p, SDII and Rx5day, had statistically increasing trends at 10% significance level (only one station). Two EPIs including CDD and PRCPTOT exhibited statistically decreasing trends at 5% significance level (only one station).

Table 3
Results of Mann-Kendall non-parametric test in EPIs (%).

Index			Positive trend	SS(5%)	SS(10%)	Negative trend	SS(5%)	SS(10%)	Stationary trend
EPIs	Fixed thresholds	CDD	38.89%	0.00%	0.00%	50.00%	5.56%	5.56%	11.11%
		CWD	16.67%	0.00%	0.00%	83.33%	0.00%	5.56%	0.00%
		R10mm	33.33%	0.00%	0.00%	66.67%	0.00%	0.00%	0.00%
		R20mm	50.00%	0.00%	0.00%	50.00%	0.00%	5.56%	0.00%
		R25mm	55.56%	0.00%	0.00%	38.89%	0.00%	0.00%	5.56%
		R50mm	50.00%	0.00%	0.00%	50.00%	0.00%	0.00%	0.00%
		R100mm	55.56%	0.00%	0.00%	27.78%	0.00%	0.00%	16.67%
		R150mm	11.11%	0.00%	0.00%	0.00%	0.00%	0.00%	88.89%
	Station-related thresholds	R95p	50.00%	0.00%	5.56%	44.44%	0.00%	5.56%	5.56%
		R99p	61.11%	5.56%	5.56%	33.33%	0.00%	0.00%	5.56%
	Non-threshold	PRCPTOT	16.67%	0.00%	0.00%	77.78%	5.56%	11.11%	5.56%
		SDII	50.00%	0.00%	5.56%	50.00%	0.00%	0.00%	0.00%
		RX1day	61.11%	0.00%	0.00%	38.89%	0.00%	0.00%	0.00%
		RX5day	50.00%	0.00%	5.56%	44.44%	0.00%	0.00%	5.56%

Note: SS indicates statistically significant at 5% and 10% significance level.

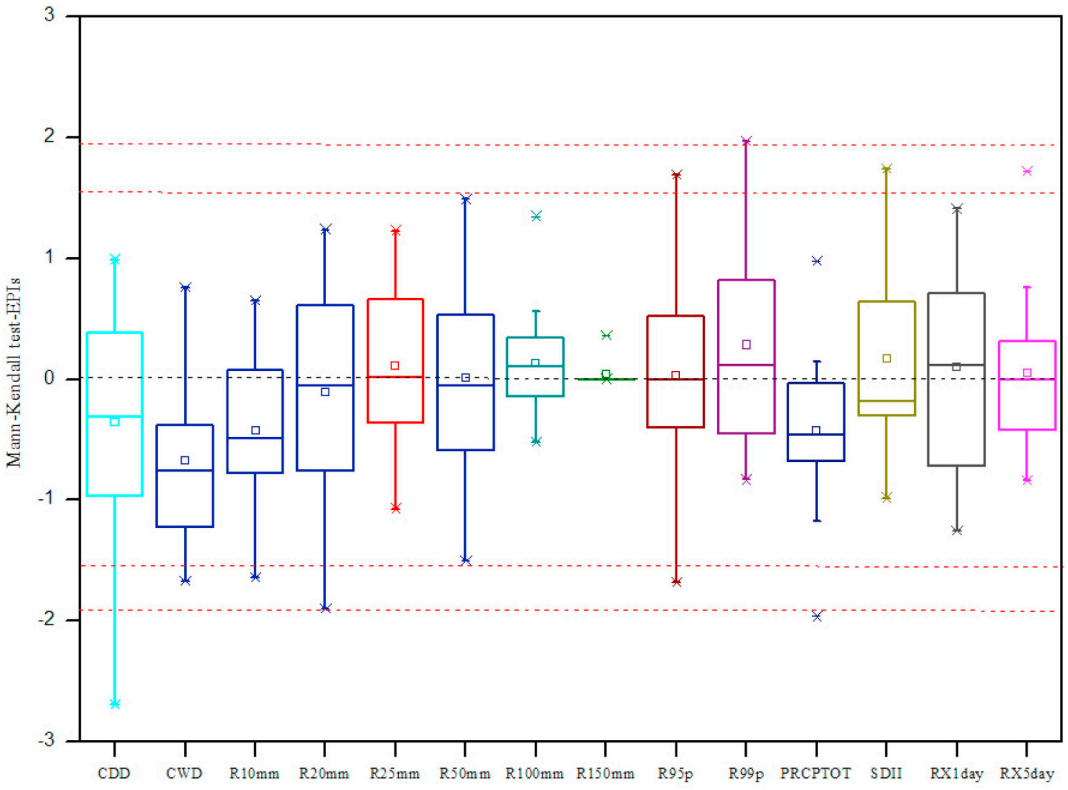

Fig. 2. Box plots of Mann-Kendall non-parametric test in EPIs.

3.2. Spatiotemporal variations of eight fixed thresholds EPIs

Fig. 3 shows the spatial distributions of trends of eight EPIs for 18 meteorological stations (as listed in Table 2) between 1969 and 2016 in the WRB. As shown in Table 3, two fixed thresholds EPIs, i.e., R25mm and R100mm showed more positive trends than negative trends. Three fixed thresholds EPIs including CDD, CWD and R10mm were decreasing trends dominated. Nine stations for other two thresholds EPIs, i.e., R20mm and R50mm showed increasing and decreasing trends, respectively.

Fig. 3a shows that spatial distribution of CDD trends for the period of 1969–2016 in the WRB. Seven stations that exhibited positive trends were scattered distributed. One station was located at the upstream, midstream and downstream of WRB, and two stations located at the JRB and BRB, respectively. Only one station named Wugong, located at the midstream of WRB had statistically decreasing trend at 5% significance level. Two stations that had stationary trends were found in the JRB and downstream of WRB, respectively. In case of CWD, more decreasing trends (83.33%) were detected than increasing trends (16.67%), and no station had stationary trend. Only three stations that located at the mainstream of WRB had increasing trends and fifteen stations had decreasing trends. Two stations named Luochuan and Huaxian, which located at the eastern part of WRB had statistically decreasing trend at 10% significance level (Fig. 3b).

Six fixed thresholds EPIs consisting of R10mm-R250mm were specially assessed using the Julian day number with precipitation above 10 mm–250 mm, respectively. As shown in Fig. 3c–h. In general, the proportions and spatial distributions of stations varied for different trends and different EPIs. More stations had decreasing trends for R10mm than other five EPIs. For R10mm, the stations that had increasing trends mainly located at the northern part of WRB, especially at the JRB and BRB. Only one station named Longxian that had increasing trend was in the midstream of WRB (Fig. 3c). Interestingly, two EPIs including R20mm and R50mm had the same number of stations (50%) that exhibited positive trends and negative trends. The spatial distributions of stations that had increasing trends were similar, mainly located at the center of WRB, especially in the JRB (Fig. 3d & f). Both R25mm and R100 had 55.56% (10 out of 18) of stations that exhibited positive trends, and the trends were scattered in the WRB. The trends were similar expect stations located at the midstream of WRB (Fig. 3e & g). R150mm was stationary trends dominated. It is worth mentioning that only two stations named Longxian and Kongtong had increasing trends for the period of 1969–2016 (Fig. 3g). We further verify the historical extreme precipitation events based on the observed daily precipitation data of above two stations. The results showed that two extreme heavy rainstorm days were found in Kongtong. The observed daily precipitation reached 159.7 mm at July 23, 1996 and 166.9 mm at July 27, 2010. One extreme heavy rainstorm day was detected in Longxian, and the observed daily precipitation was 214.6 mm at July 23, 2010. Several previous studies also showed that the WRB was subjected to severe rainstorm and flooding, which concurred with above results (Liu et al., 2017).

3.3. Spatiotemporal variations of two station-related thresholds EPIs

Fig. 4 shows the spatial distributions of trends of two station-related thresholds EPIs, i.e., R95p and R99p, for the period of 1969–2016 in the WRB. Generally, R95p and R99p had similar spatial distributions of trends. Both EPIs were positive trends dominated, 50% for R95p and 61.11% for R99p. For R95p, three stations had statistically significant positive, negative and stationary trends, respectively. The stations that exhibited different trends distributed unevenly in the WRB (Fig. 4a). In case of R99p, more stations had positive trends than those of R95p. All stations located at the JRB and BRB had positive trends, and one station named Huanxian has statistically significant increasing trend at 5% significance level (Fig. 4b).

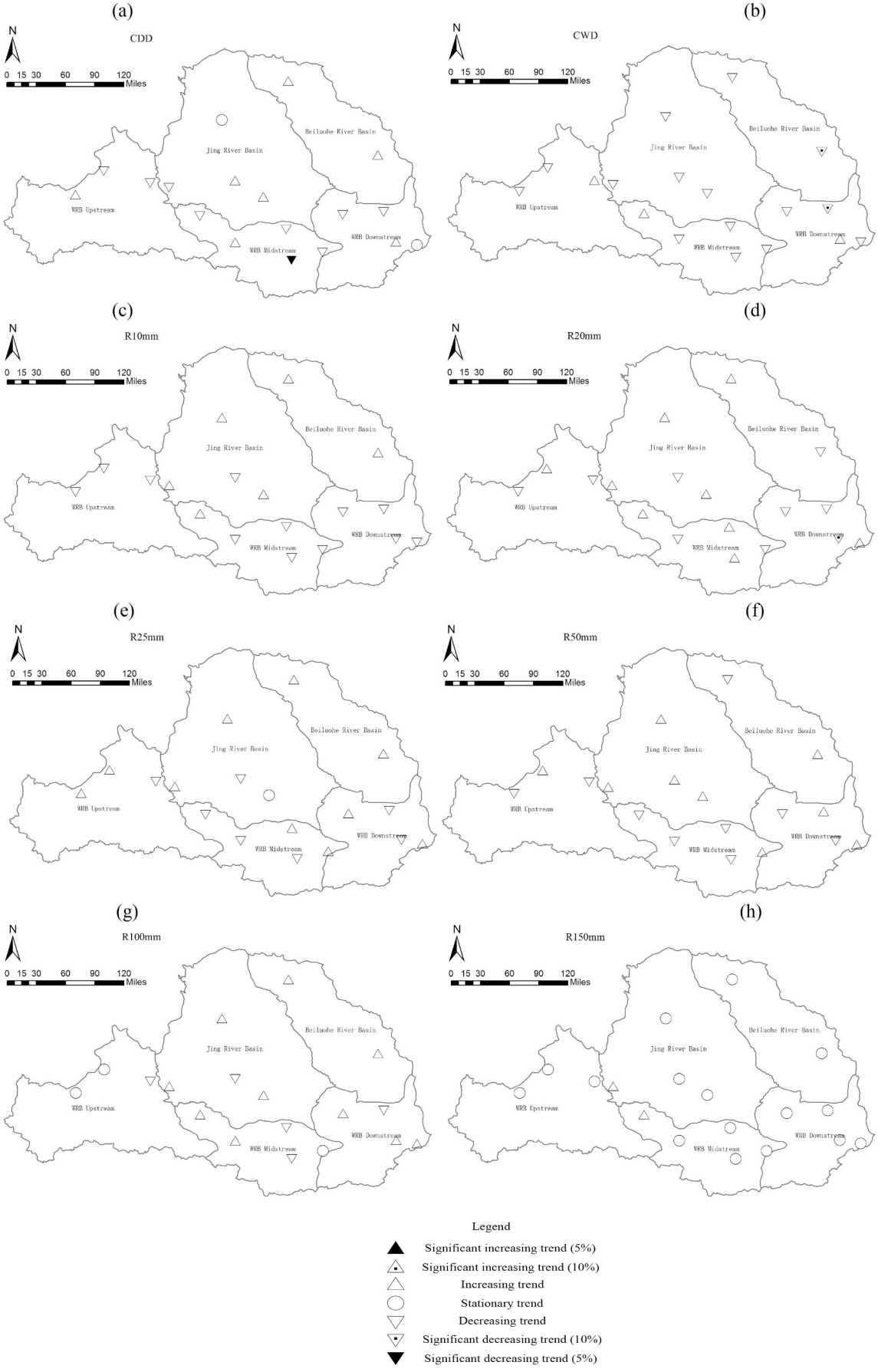

Fig. 3. Trends of eight fixed thresholds EPIs.

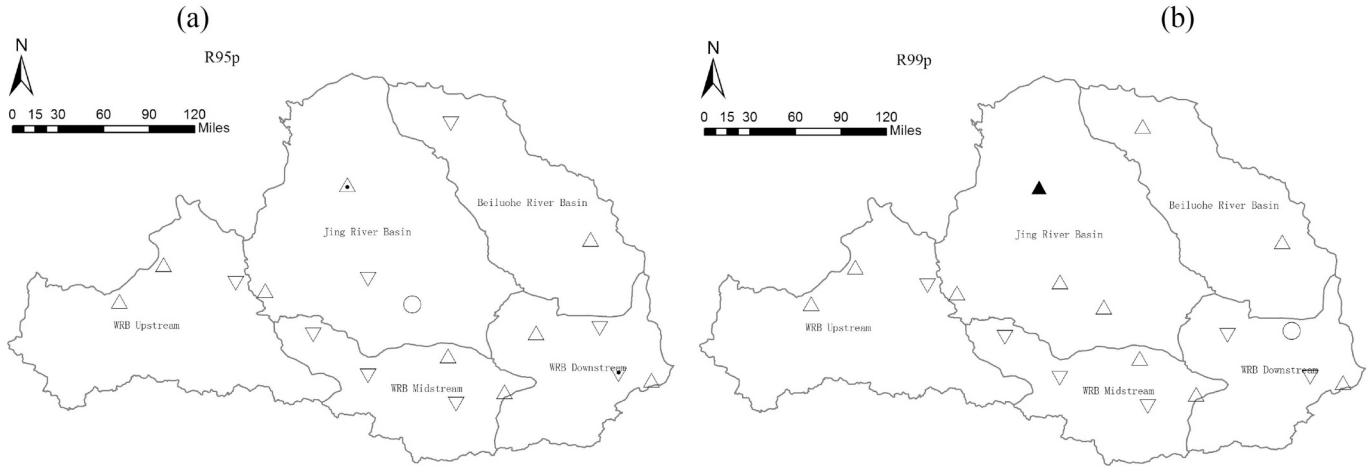

Fig. 4. Trends of two station-related thresholds EPIs (The legend is the same as Fig. 3).

3.4. Spatiotemporal variations of four non-threshold EPIs

Fig. 5 shows the spatial distributions of trends of four non-threshold EPIs for the period of 1969–2016 in the WRB. The annual total wet-day precipitation was negative trends dominated. Three stations (16.67%) that had increasing trends were located at the JRB. Stations located at the mainstream of WRB had decreasing trends, including one station named Huanxian that had statistically significant decreasing trend at 5% significance level (Fig. 5a). In case of SDII, 50% (nine out of 18) stations had positive trends in the WRB, which mainly distributed at the northern of WRB (Fig. 5b).

For other two monthly maximum 1-day and 5-day precipitation, more stations had positive trends than negative trends. In case of Rx1day, eleven stations had positive trends and seven stations had negative trends. The stations that had increasing trends mainly located at the center of WRB, especially, in the JRB. However, only one out of five stations had increasing trends in the midstream of WRB. No stations had statistically significant trends at both 5% and 10% significance levels (Fig. 5c). Similar with that of Rx1day, the trends were spatially distributed and scattered for Rx5day. Moreover, one station named

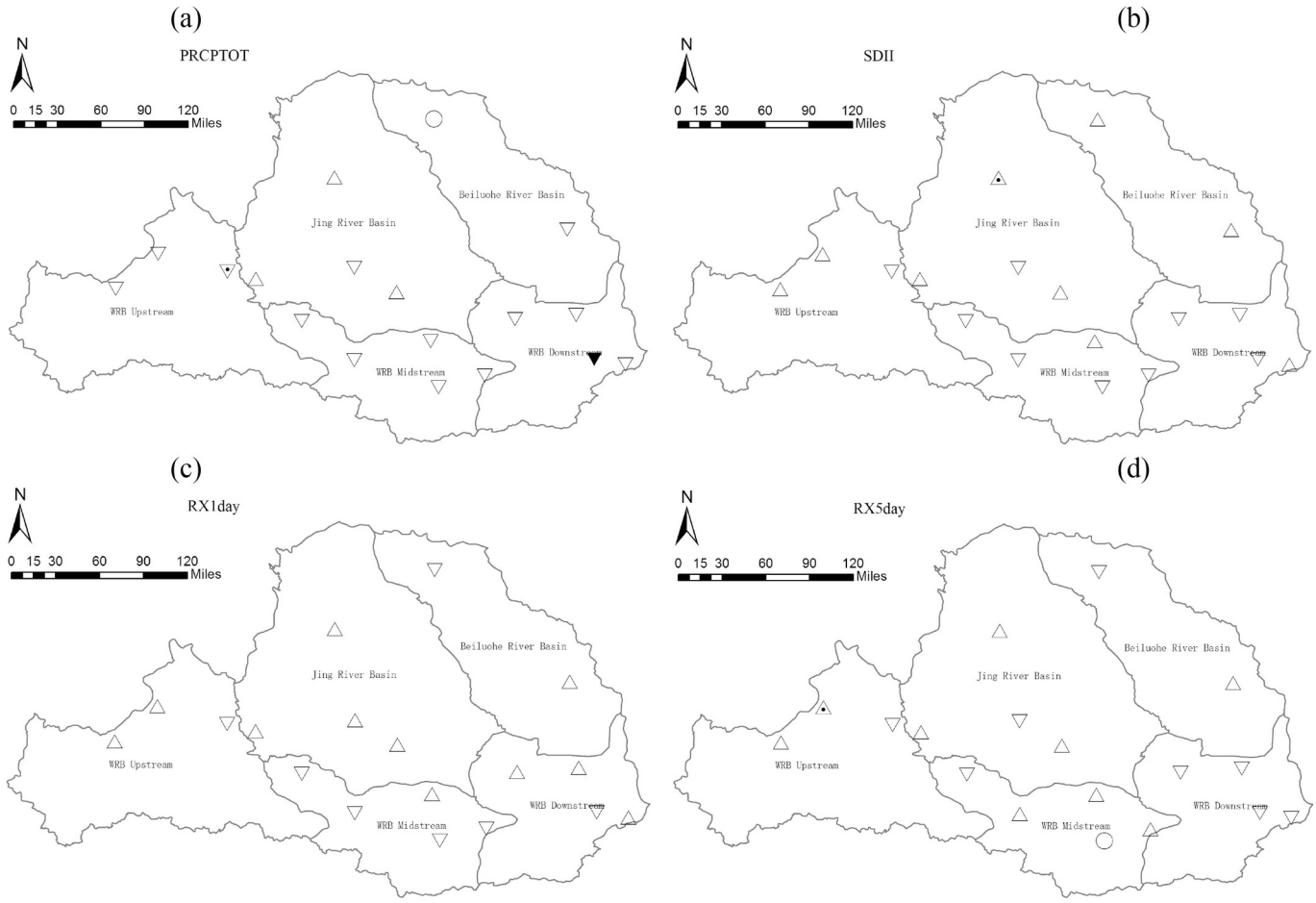

Fig. 5. Trends of four non-threshold EPIs (The legend is the same as Fig. 3).

Table 4
Cross correlation coefficients between different EPIs.

EPIs	CDD	CWD	R10mm	R20mm	R25mm	R50mm	R95p	R99p	PRCPTOT	SDII	RX1day	RX5day
CDD	1	−0.2535	−0.0435	0.0591	0.0321	−0.0014	−0.0043	0.0282	−0.0595	0.1131	0.1074	−0.0091
CWD		1	0.4870*	0.3614*	0.3378*	0.0496	0.2317	0.0268	0.4965*	0.1211	−0.0694	0.4915*
R10mm			1	0.8962*	0.8081*	0.3528*	0.6060*	0.3461*	0.9555*	0.6492*	0.2403	0.5129*
R20mm				1	0.9574*	0.5537*	0.8237*	0.5559*	0.9413*	0.8359*	0.4412*	0.6367*
R25mm					1	0.6198*	0.9033*	0.6309*	0.8904*	0.8477*	0.5218*	0.6686*
R50mm						1	0.8174*	0.9605*	0.5018*	0.5950*	0.6582*	0.6038*
R95p							1	0.8264*	0.7576*	0.8382*	0.7101*	0.7492*
R99p								1	0.5004*	0.6313*	0.7507*	0.6295*
PRCPTOT									1	0.6918*	0.3808*	0.6321*
SDII										1	0.6356*	0.6407*
RX1day											1	0.6199*
RX5day												1

* Indicate statistically significant at 5% significant level.

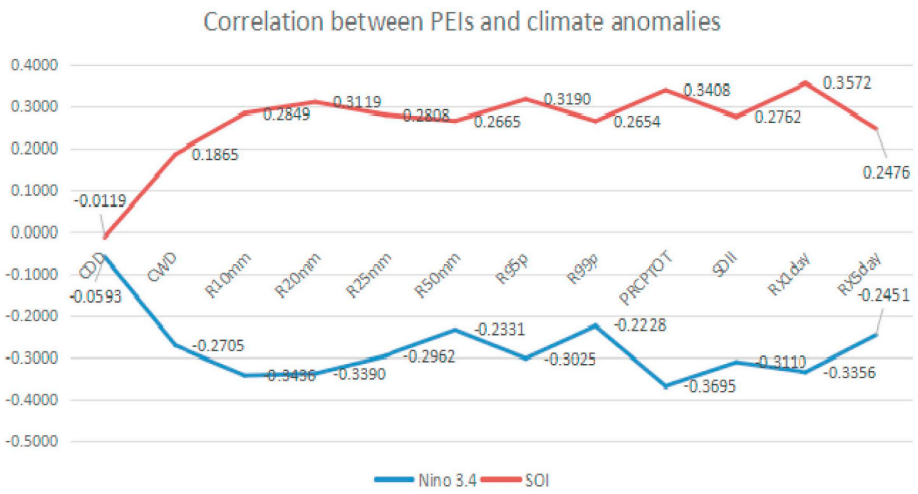

Fig. 6. Pearson's correlation coefficients between EPIs and two ENSO anomalies (Niño 3.4 and SOI).

Wugong located at the most south of WRB had stationary trend, for the period of 1969–2016 (Fig. 5d).

3.5. Correlation analysis of EPIs and climate anomalies

To further study the possible relationships between extreme precipitation events and ENSO, the PCA was used to extract the dominate mode of variability of fourteen EPIs from 18 stations for the period of 1969–2016 in the WRB. The leading principal component (PC1) was used as a substitution for each EPIs, because the PC1 of the each EPIs explained the largest proportion of the total variability. For example, the PC1 of the CDD explained 52.13% of variability of 18 stations.

Table 4 shows the correlation coefficients between different PC1 of fourteen EPIs for the period of 1969–2016 in the WRB. The results indicated that all PC1 of EPIs except CDD and CWD were mainly statistically positive correlated with each other. The highest correlation coefficient was detected between PC1 of R50mm and R99p (0.9605), followed by PC1 of R20mm and R25mm (0.9574), and PC1 of R10mm and PRCPTOT (0.9555). The results mainly concurred with the results of Mann-Kendall test, as shown in Table 3 and Figs. 3–5. Taking PC1 of R50mm and R99p for examples, the proportions of stations that exhibited positive trends had little difference, 50% for R50mm and 61.11% for R99p. The spatial distributions of trends of R50mm (Fig. 3f) and R99p (Fig. 4b) were also similar.

To quantitatively investigate the linear relationships between EPIs and ENSO, Pearson's correlation (ρ) between PC1 of fourteen EPIs and two climate anomalies including Niño 3.4 and SOI were analyzed, as shown in Fig. 6. In general, all PC1s of EPIs expect CDD and CWD were strongly correlated to two climate anomalies. All PC1s of EPIs were negatively correlated with Niño 3.4, indicating that the Niño 3.4 had negative impacts on the EPIs in the WRB, and vice-versa for SOI. Among the eight fixed thresholds EPIs, ρ between PC1 of R20mm and two climate anomalies was the strongest, and R95p for station-related thresholds EPIs. In case of non-threshold EPIs, both PC1 of PRCPTOT and Rx1day were stronger correlated with two climate anomalies than other two EPIs. Thus, four typical EPIs including R20mm, R95p, PRCPTOT and Rx1day were selected to further reveal the nonlinear relationships between PC1 of EPIs and two climate anomalies using wavelet analysis in the following section.

3.6. Wavelet coherence and phase difference between EPIs and Niño 3.4

Fig. 7 shows the wavelet coherence and phase difference between PC1 of four typical EPIs and Niño 3.4. The thick enclosed areas in Fig. 7 signify statistically significant coherence at 5% significance level with respect to a red noise based on Monte Carlo simulation method (Grinsted et al., 2004; Jevrejeva et al., 2003). The arrows indicate that the wavelet coherence between PC1 of EPIs and Niño 3.4 are > 0.5, and represent the phase difference of oscillation. The arrow towards right shows in-phase coherence between PC1 of EPIs and Niño 3.4, and vice versa for anti-phase.

Fig. 7a shows 1–6 year cycles isolated coherence between PC1 of R20mm and Niño 3.4, which were mainly anti-phase. Statistically significant wavelet coherences were mainly detected at 4–6 year for the period of 1980–2010. 1–2 year statistically significant wavelet coherences were mainly found before 1990, especially, in 1970s. However, the areas that had statistically significant wavelet coherences in 1970s were located on the border or outside of the cone of influence (COI),

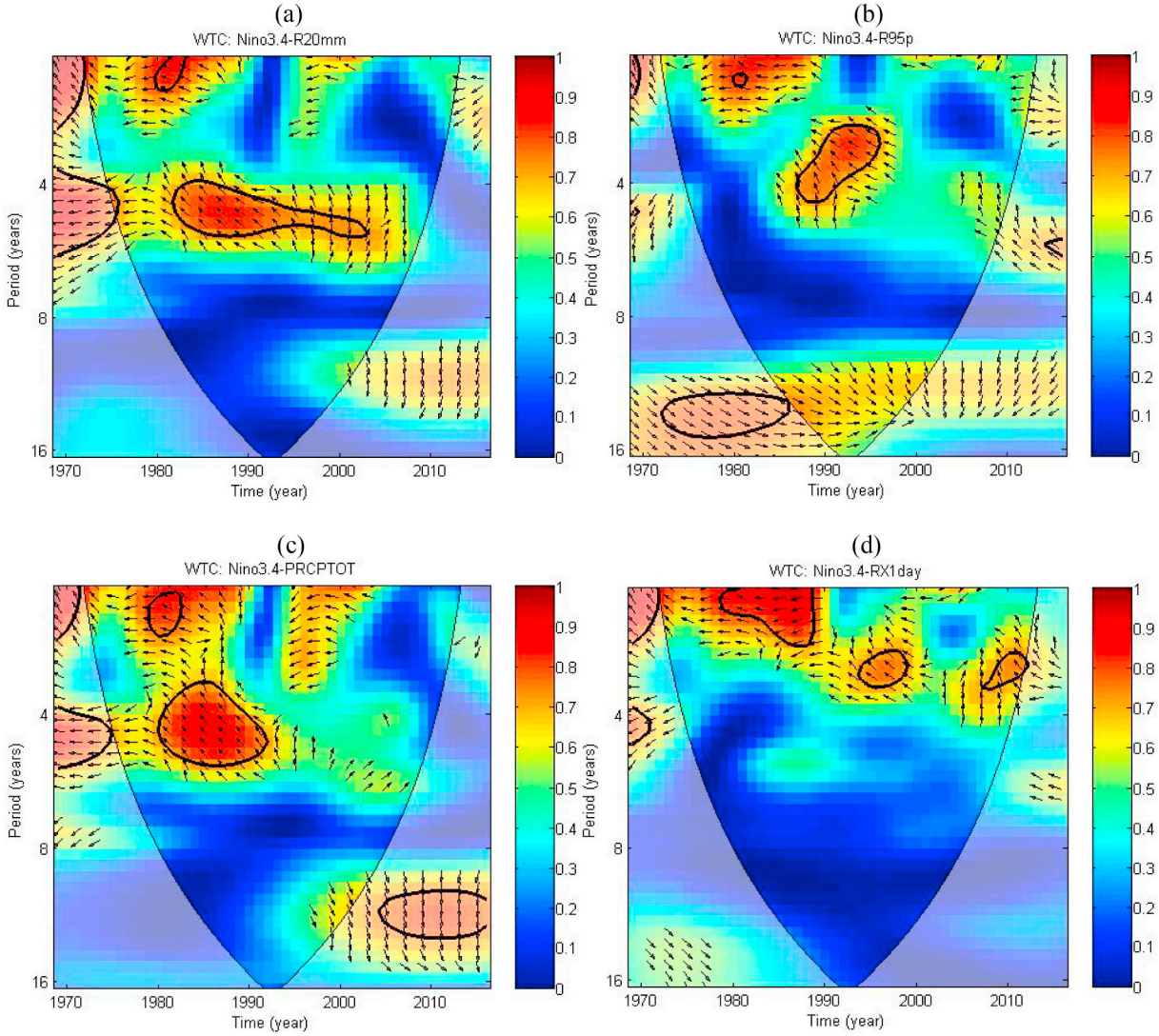

Fig. 7. Wavelet coherence and phase difference between PC1 of typical EPIs and Niño 3.4: (a) R10mm, (b) R95p, (c) PRCPTOT, (d) RX1day for the period of 1969–2016.

which should be explained cautiously. Fig. 7b shows the wavelet phase difference between PC1 of R95p and Niño 3.4. A relative weak wavelet coherence centered at 4-year cycle was detected in 1990s, and the coherences were also anti-phase dominated. Some scattered coherences also appeared at different periods, especially nearly 10–16 year cycles coherence throughout the study period. However, the areas that had statistically significant wavelet coherences were mainly located outside of COI. The phase difference transformed from nearly -45° in 1970s to -90° in 2000s and finally -135° in 2010s.

The wavelet coherence and phase difference between PC1 of PRCPTOT and Niño 3.4 (Fig. 7c) were very similar with those of PC1 of R20mm and Niño 3.4 (Fig. 7a). Areas that had statistically significant wavelet coherences were mainly located at 4–6 year cycles in 1980s and 1990s. Relative weak and scattered wavelet coherences were found at 1–2 year cycles. It is noteworthy that an approximate 12 year cycle statistically significant coherence was detected after 2000. However, the coherence was outside of the COI, which again need to be interpreted carefully.

The statistically significant wavelet coherences between Rx1day and Niño 3.4 were mainly found at small time period, such as 1–2 year cycles isolated coherence before 1990, 2–4 year cycles coherence in 1990s and 2010s, as shown in Fig. 7d. However, the phase differed at different periods. For example, the coherences were anti-phase dominated at small period, whilst the coherences changed to in-phase at relatively large period in 1970s.

3.7. Wavelet coherence and phase difference between EPIs and SOI

Fig. 8 shows the wavelet coherence and phase difference between PC1 of four typical EPIs and SOI for the period of 1969–2016 in the WRB. The wavelet coherence between PC1 of R20mm and SOI was somewhat similar with that of PC1 of R20mm and Niño 3.4 (Fig. 7a). Scattered coherences mainly of 1–8 year cycles were detected throughout the study period, with a 4–6 year cycles statistically significant coherences mainly during 1980–2000, and strong coherences prior to 1980, which again lies at the border or outside of the COI and thus it may be subject to errors. To the contrary, the phase differences of coherence between PC1 of R20mm and SOI are in phase, especially during periods of significant coherence (Fig. 8a).

As expected, the wavelet coherences between PC1 of R95p and SOI were similar with that of R95p and Niño 3.4 (Fig. 7b). Fig. 8b shows scattered statistically significant coherences between them at nearly 1–2 year cycles in 1980s and 2–5 year cycles in 1990s, and an inter-decadal cycle almost throughout the study period. Generally, PC1 of R95p and SOI had been in phase with each other within the COI, and the inter-decadal coherences were mainly anti-phase.

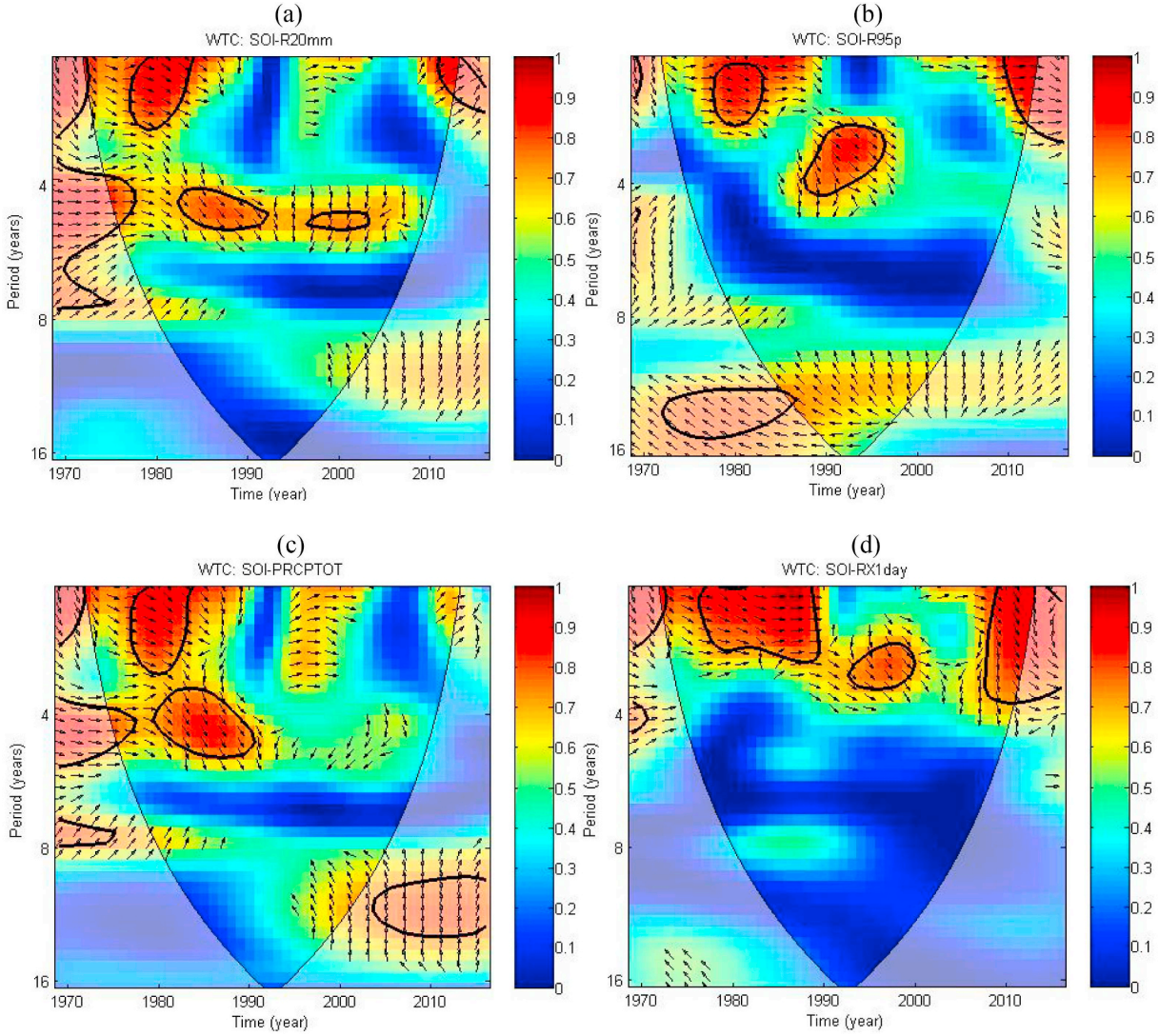

Fig. 8. Wavelet coherence and phase difference between PC1 of typical EPIs and SOI: (a) R10mm, (b) R95p, (c) PRCPTOT, (d) RX1day for the period of 1969–2016.

Fig. 8c shows the wavelet coherences and phase differences between PC1 of PRCPTOT and SOI, with intensive statistically significant coherences mainly of 1–6 year cycles before 1990, and an inter-decadal cycle which mainly outside of COI. In contrast with that of PC1 of PRCPTOT and Niño 3.4 (Fig. 7c), two signals were mainly in phase at inter-annual oscillation and anti-phase at inter-decadal oscillation, but the latter mainly outside of COI.

The wavelet coherences between PC1 of Rx1day and SOI (Fig. 8d) were similar with those of PC1 of Rx1day and Niño 3.4 (Fig. 7d). The statistically significant coherence was mainly at inter-annual oscillation of 1–4 year cycles throughout the study period. However, the phase differences of the strong coherence had essentially been of in phase, indicating that the SOI had positive impacts on the Rx1day.

4. Discussion

Our results showed that the spatial and temporal change characteristics varied for different EPIs and meteorological stations, as shown in Table 3 and Figs. 3–5. In general, several EPIs, such as wet/dry days (CWD & CDD) and annual total wet-day precipitation were mainly negative trends dominated, and other EPIs were positive trends dominated, indicating that the extreme precipitation events have mainly increased. The synthesis report of IPCC AR5 found that the precipitation extremes had mainly increased around the world, especially, in the Northern Hemisphere, which caused more precipitation related disaster (IPCC, 2014). The results are mainly consistent with previous studies. For example, Liu et al. (2017) investigated the change patterns and stationary of extreme precipitation events using eight precipitation indices, and further analyzed the teleconnections of precipitation extremes to Pacific Decadal Oscillation (PDO) and ENSO using cross wavelet approach, based on daily precipitation for the period of 1960–2010 in the WRB of China. The results found that the precipitation extremes had different trends for different stations. However, the CWD had decreasing trends dominated at 5% significant level, which mainly concurred with the results revealed in the paper (Table 3).

We further investigate the teleconnections of extreme precipitation events to ENSO, represented by Niño 3.4 and SOI, to reveal the change mechanism of precipitation extremes in the WRB. In general, relationships between different EPIs and global climate anomalies are complex and unstable at both inter-annual and inter-decadal cycles using correlation and wavelet analysis. The linear and nonlinear relationships between them likely vary in both time and frequency. However, the results of linear relationships using Pearson's correlation (Fig. 6) and nonlinear relationships using wavelet analysis (Figs. 7 & 8) between PC1 of typical EPIs and two climate anomalies are mainly consistent with each other. The in phase (anti-phase) differences of wavelet coherence generally concur with positive (negative) correlation

coefficients. For example, the PC1 of R20mm is positively and significantly related to Niño 3.4 ($\rho = -0.3390$), as shown in Fig. 6, and phase differences of wavelet coherence between them shown in Fig. 7a are mainly in opposite modes for the period of 1969–2016. In contrast, SOI is negatively and significantly correlated to PC1 of R20mm ($\rho = -0.3119$), and the phase differences between them are in phase dominated (Fig. 8a). Similar results are also detected for other EPIs (Fig. 6, Fig. 7b–d & Fig. 8b–d). The linear and nonlinear telecomnnections of extreme precipitation events to ENSO indicated that it is possible to estimate the extreme precipitation events in the WRB using global climate anomalies ENSO as potential predictors. However, the mechanisms of extreme precipitation events in certain catchment are complex. Except for ENSO, many global climate anomalies such as Pacific decadal Oscillation (PDO) (Mantua and Hare, 2002), Pacific/North American (PNA) (Gan et al., 2002), North Atlantic Oscillation (NAO) (Hurrell and Vanloon, 1997) also exert influences on the regional precipitation, which have been revealed by Gan et al. (2007) and Jiang et al. (2016). Thus, it should be more reasonable to include the combined effects of multiple global climate anomalies to predict regional extreme precipitation events.

Results of Fig. 6 indicated that the Niño 3.4 was negatively correlated to each EPIs, but the SOI was positively correlated to each EPIs, except CDD. The results concur with Jiang et al. (2014) who revealed that the results between correlation analysis and wavelet coherence analysis mainly concurred with each other. The in phase wavelet coherence differences were mainly consistent with positive correlations, and vice versa. The results found that the correlations between different PCs of seasonal precipitation and Niño 3 were mainly negative dominated at different bands, and mainly positive correlated to SOI, especially for PC1 of seasonal precipitation. Composite analysis was recommended to estimate the isolated influences of extreme phases of ENSO on EPIs, because different phases of ENSO might have opposite effects due to tropical clouds and circulation (Su and Jiang, 2013; Jiang et al., 2017b). According to the findings of Gan et al. (2007), ENSO including Niño 3 and SOI had strong impacts on the winter precipitation of southwest Canada with respect to other several climate anomalies. Different ENSO episodes were closely related to different phase of SOI. For example, the El Niño (La Niña) episodes are correlated with negative (positive) SOI, indicating that lower (higher) pressure over Tahiti and higher (lower) pressure in Darwin (IPCC, 2014). Jiang et al. (2017b) detected that the ENSO had greater impacts on annual total wet-day precipitation than other precipitation extremes using correlation and composite analysis. The results were consistent with our results as shown in Fig. 6, which showed that ρ between Niño 3.4 and PRCPTOT was higher than other EPIs. Especially, using future simulations of climate models, the IPCC AR5 projected that the ENSO related regional precipitation variations would probable intensify (IPCC, 2014), which will be discussed in our further work.

5. Conclusions

Using the Mann-Kendall non-parametric test, the paper assessed the extreme precipitation events with 14 EPIs, and investigated the spatiotemporal variability of EPIs during 1969–2016 in the WRB, located at the west-central of China, which is also the largest tributary of Yellow River. To further reveal the change mechanism of variability of extreme precipitation events, we further investigated the linear and nonlinear relationships between EPIs and ENSO, using Niño 3.4 and SOI as alternative climate anomalies. Based on the above results and discussion, our mainly findings are summarized as follows:

(1) Seven change characteristics including positive, negative, stationary, statistically significant positive or negative trends at both 5% and 10% significance levels were used to analyze the trends of different EPIs. In general, the change characteristics of precipitation extremes varied for different EPIs, different areas and different meteorological stations for the period of 1969–2016 in the WRB of China (Table 3 & Fig. 2). Four EPIs including CDD, CWD, R10mm and PRCPTOT were decreasing trends dominated, and six EPIs were positive trends dominated. Other three EPIs including R20mm, R50mm and SDII had equal proportions of stations that exhibited increasing and decreasing trends. Two stations incuding Kongtong and Longxian had increasing trends in R150mm, which were further verified with historical extreme precipitation events (Fig. 3h). Eleven out of eighteen (61.11%) of stations had increasing trends for two EPIs including R99p and Rx1day, which also had the highest proportion of positive trend (Table 3). On the contrary, the proportion of stations with negative trends of three EPIs sorted as CWD (83.33%), PRCPTOT (77.78%) and R10mm (66.67%) were in excess of 50%.

(2) The spatial distributions of increasing and decreasing trends for different EPIs were irregular and scattered, as shown in Figs. 3–5. The spatial distributions of stations with increasing trends were scattered for CDD (Fig. 3a), and mainly located at the mainstream of WRB for CWD (Fig. 3b). In case of R10mm, the stations exhibited increasing trends mainly located at the JRB and BRB (Fig. 3c). For other fixed thresholds EPIs, the trends were largely similar. The stations that had increasing trends were mainly in the center of WRB, especially in the JRB (Fig. 3d-g). In case of two station-related thresholds EPIs, R95p mainly had uneven spatial distribution of trends (Fig. 4a), and the stations that had positive trends mainly located at the JRB and BRB for R99p (Fig. 4b). For PRCPTOT, three stations that had increasing trends were in the JRB (Fig. 5a). The stations with positive trends were mainly located at the northern of WRB (Fig. 5b). In case of two non-threshold EPIs, the positive trends were mainly distributed in the center of WRB for both Rx1day and Rx5day (Fig. 5c & d).

(3) The linear and nonlinear relationships between EPIs and ENSO were further investigated using Pearson's correlation, wavelet coherence and phase difference. All PC1 of EPIs except consecutive wet/dry days were statistically positive correlated with each other (Table 4), indicating that it is feasible to use EPIs to assess extreme precipitation events. Niño 3.4 was negatively correlated with all fourteen EPIs and SOI was positively correlated with all EPIs except CDD, indicating that Niño 3.4 exerted negative influences on the extreme precipitation events in the WRB, and vice-versa for SOI (Fig. 6). In general, the Niño 3.4 and SOI had similar wavelet coherence and opposite phase difference with PC1 of four typical EPIs. The statistically significant wavelet coherences were mainly detected at inter-annual year cycles nearly at 1–8 year. Inter-decadal oscillations at approximately centered 12 year were found between Niño 3.4 (SOI) and two typical EPIs including R95p and RECPTOT. However, the statistically significant wavelet coherences were mainly located at the border or outside of the COI, which should be explained in cautious (Figs. 7 & 8). The phase differences between Niño 3.4 and PC1 of EPIs were anti-phase dominated, and in-phase dominated between SOI and PC1 of EPIs, which concurred with the results of correlation analysis (Fig. 6).

Our findings above provide assessment of extreme precipitation events under changing environment, which should be useful for the water resources planning and management in the WRB. Especially, we further investigated the possible climate change impacts of ENSO on the extreme precipitation events. It expands our knowledge to estimate regional extreme precipitation events using global climate anomalies such as ENSO as potential predictors. Our future work will focus on the projected future trends of extreme precipitation events in the WRB using climate models and prediction of extreme precipitation events using multiple global climate anomalies.

Acknowledgments

The study was partly funded by the National Key Research and Development Program of China (2016YFC0401409), National Natural Science Foundation of China (51509201, 51679188 and 41471451), Natural Science Basic Research Plan in Shaanxi Province of China (2018JM5031) and Research Foundation of State Key Laboratory of Eco-hydraulics in Northwest Arid Region of China (2017ZZKT-6, 2017KFKT-1). The daily precipitation data were obtained from the China Meteorological Data Sharing Service System at http://cdc.nmic.cn. The Niño 3.4 was got from National Weather Service CPC of NOAA at http://www.cpc.ncep.noaa.gov/data/indices/ and the SOI was downloaded from CRU at https://crudata.uea.ac.uk/cru/data/soi/. The EPIs were calculated using RClimDex obtained from http://etccdi.pacificclimate.org. The wavelet analysis package was developed by Drs. Christopher Torrence and Gilbert P. Compo, available at http://atoc.colorado.edu/research/wavelets/. The authors thank the editor and anonymous reviewers for their valuable comments and suggestions.

References

Alexander, L.V., Zhang, X., Peterson, T.C., Caesar, J., Gleason, B., Klein Tank, A.M.G., Haylock, M., Collins, D., Trewin, B., Rahimzadeh, F., Tagipour, A., Rupa Kumar, K., Revadekar, J., Griffiths, G., Vincent, L., Stephenson, D.B., Burn, J., Aguilar, E., Brunet, M., Taylor, M., New, M., Zhai, P., Rusticucci, M., Vazquez-Aguirre, J.L., 2016. Global observed changes in daily climate extremes of temperature and precipitation (1984–2012). J. Geophys. Res. 111, D05109.

Allan, R.P., Soden, B.J., 2008. Atmospheric warming and the amplification of precipitation extremes. Science 321, 1481–1484.

Cavanaugh, N.R., Gershunov, A., Panorska, A.K., Kozubowski, T.J., 2015. The probability distribution of intense daily precipitation. Geophys. Res. Lett. 42, 1560–1567.

Croitoru, A.E., Chiotoroiu, B.C., Todorova, V.I., Torica, V., 2013. Changes in precipitation extremes on the Black Sea Western Coast. Glob. Planet Change 102, 10–19.

Easterling, D.R., Evans, J.L., Groisman, P.Y., Karl, T.R., Kunkel, K.E., Ambenje, P., 2000. Observed variability and trends in extreme climate events: a brief review. B. Am. Meteorol. Soc. 81, 417–425.

Emori, S., 2005. Dynamic and thermodynamic changes in mean and extreme precipitation under changed climate. Geophys. Res. Lett. 32, L17706.

Gan, T.Y., Wang, Q., Seneka, M., 2002. Correlation dimensions of climate subsystems and their geographic variability. J. Geophys. Res. 107 (D23), 4728.

Gan, T.Y., Gobena, A.K., Wang, Q., 2007. Precipitation of southwestern Canada: wavelet, scaling, multifractal analysis, and teleconnection to climate anomalies. J. Geophys. Res. 112, D10110.

Grimm, A.M., Tedeschi, R.G., 2009. ENSO and extreme rainfall events in South America. J. Clim. 22, 1589–1609.

Hamed, K.H., 2009. Exact distribution of the Mann-Kendall trend test statistic for persistent data. J. Hydrol. 365, 86–94.

Hurrell, J.W., Vanloon, H., 1997. Decadal variations in climate associated with the North Atlantic oscillation. Clim. Chang. 36, 301–326.

IPCC, 2014. In: Core Writing Team, Pachauri, R.K., Meyer, L.A. (Eds.), Climate Change (2014) Synthesis Report. Contribution of Working Groups I, II and III to the Fifth Assessment Report of the Intergovernmental Panel on Climate Change. IPCC, Geneva, Switzerland.

Jevrejeva, S., Moore, J.C., Grinsted, A., 2003. Influence of the arctic oscillation and El Nino-Southern Oscillation (ENSO) on ice conditions in the Baltic Sea: The wavelet approach. J. Geophys. Res. 108 (D21), 4677.

Jiang, R., Xie, J., Li, J., 2013. Application of World Wind on hydrologic monitoring and simulation in Shaanxi province, China. Disaster Adv. 6, 33–47.

Jiang, R., Gan, T.Y., Xie, J., Wang, N., 2014. Spatiotemporal variability of Alberta's seasonal precipitation, their teleconnection with large-scale climate anomalies and sea surface temperature. Int. J. Climatol. 34, 2899–2917.

Jiang, R., Xie, J., He, H., Luo, J., Zhu, J., 2015. Use of four drought indices for evaluating drought characteristics under climate change in Shaanxi, China: 1951–2012. Nat. Hazards 75, 2885–2903.

Jiang, R., Xie, J., He, H., Kuo, C.-C., Zhu, J., Yang, M., 2016. Spatiotemporal variability and predictability of Normalized Difference Vegetation Index (NDVI) in Alberta, Canada. Int. J. Biometeorol. 60, 1389–1403.

Jiang, R., Gan, T.Y., Xie, J., Wang, N., Kuo, C.-C., 2017a. Historical and potential changes of precipitation and temperature of Alberta subjected to climate change impact: 1900–2100. Theor. Appl. Climatol. 127, 725–739.

Jiang, R., Xie, J., Zhao, Y., He, H., He, G., 2017b. Spatiotemporal variability of extreme precipitation in Shaanxi province under climate change. Theor. Appl. Climatol. 130, 831–845.

Li, W., Zhai, P., Cai, J., 2011. Research on the relationship of ENSO and the frequency of extreme precipitation events in China. Adv. Clim. Chang. Res. 2, 101–107.

Liu, S., Huang, S., Huang, Q., Xie, Y., Leng, G., Luan, J., Song, X., 2017. Identification of the non-stationarity of extreme precipitation events and correlations with large-scale ocean-atmospheric circulation patterns: a case study in the Wei River Basin, China. J. Hydrol. 548, 184–195.

Mantua, N.J., Hare, S.R., 2002. The Pacific decadal oscillation. J. Oceanogr. 58, 35–44.

Min, S.-K., Zhang, X., Zwiers, F.W., Hegerl, G.C., 2011. Human contribution to more-intense precipitation extremes. Nature 470, 378–381.

Ropelewski, C.F., Jones, P.D., 1987. An extension of the Tahiti-Darwin southern oscillation index. Mon. Weather Rev. 115, 2161–2165.

Schubert, S.D., Chang, Y., Suarez, M.J., Pegion, P.J., 2008. ENSO and wintertime extreme precipitation events over the contiguous United States. J. Clim. 21, 22–39.

Shadmani, M., Marofi, S., Roknian, M., 2012. Trend analysis in reference evapotranspiration using Mann-Kendall and Spearman's Rho tests in arid regions of Iran. Water Resour. Manag. 26, 211–224.

Shimizu, M.H., Ambrizzi, T., Liebmann, B., 2017. Extreme precipitation events and their relationship with ENSO and MJO phases over northern South America. Int. J. Climatol. 37, 2977–2989.

Singh, C.V., 2006. Pattern characteristics of Indian monsoon rainfall using principal component analysis (PCA). Atmos. Res. 79, 317–326.

Su, H., Jiang, J.H., 2013. Tropical clouds and circulation changes during the 2006/07 and 2009/10 El Niños. J. Clim. 26, 399–413.

Sun, W.Y., Mu, X.M., Song, X.Y., Wu, D., Cheng, A.F., Qiu, B., 2016. Changes in extreme temperature and precipitation events in the Loess Plateau (China) during 1960-2013 under global warming. Atmos. Res. 168, 33–48.

Torrence, C., Compo, G.P., 1998. A practical guide to wavelet analysis. B. Am. Meteorol. Soc. 79, 61–78.

Torrence, C., Webster, P.J., 1999. Interdecadal changes in the ENSO-monsoon system. J. Clim. 12, 2679–2690.

Trenberth, K.E., 1997. The definition of El Niño. B. Am. Meteorol. Soc. 78, 2771–2777.

Utsumi, N., Seto, S., Kanae, S., Maeda, E.E., Oki, T., 2011. Does higher surface temperature intensify extreme precipitation? Geophys. Res. Lett. 38, L16708.

Varotsos, C.A., 2013. The global signature of the ENSO and SST-like fields. Theor. Appl. Climatol. 113, 197–204.

Varotsos, C.A., Cracknell, A.P., Efstathiou, M.N., 2018. The global signature of the El Niño/La Niña southern oscillation. Int. J. Remote Sens. 39, 5965–5977.

Wang, X., Hou, X., Wang, Y., 2017. Spatiotemporal variations and regional differences of extreme precipitation events in the Coastal area of China from 1961 to 2014. Atmos. Res. 197, 94–104.

Yue, S., Wang, C.Y., 2002. Applicability of prewhitening to eliminate the influence of serial correlation on the Mann-Kendall test. Water Resour. Res. 38, 1068.

Yue, S., Pilon, P., Cavadias, G., 2002. Power of the Mann-Kendall and Spearman's rho tests for detecting monotonic trends in hydrological series. J. Hydrol. 259, 254–271.

Zhai, P., Zhang, X., Wan, H., Pan, X., 2005. Trends in total precipitation and frequency of daily precipitation extremes over China. J. Clim. 18, 1096–1108.

Zhang, X., Yang, F., 2004. RClimDex (1.0) User Manual. Climate Research Branch Environment, Canada, pp. 22.

Zhang, X.B., Hogg, W.D., Mekis, E., 2001. Spatial and temporal characteristics of heavy precipitation events over Canada. J. Clim. 14, 1923–1936.

Zhang, Q., Li, J.F., Singh, V.P., Xu, C.Y., 2013. Copula-based spatio-temporal patterns of precipitation extremes in China. Int. J. Climatol. 33, 1140–1152.

Ziegler, A.D., 2012. Reduce urban flood vulnerability. Nature 481, 145.